HHS Public Access

Author manuscript

Nat Cell Biol. Author manuscript; available in PMC 2017 July 23.

Published in final edited form as:

Nat Cell Biol. 2017 February ; 19(2): 85–93. doi:10.1038/ncb3463.

Actin Dynamics and Competition for Myosin Monomer Govern the Sequential Amplification of Myosin Filaments

Jordan R. Beach[1], **Kyle S. Bruun**[1], **Lin Shao**[2], **Dong Li**[2], **Zac Swider**[1], **Kirsten Remmert**[1], **Yingfan Zhang**[3], **Mary A. Conti**[3], **Robert S. Adelstein**[3], **Nasser M. Rusan**[1], **Eric Betzig**[2], and **John A. Hammer**[1]

[1]Cell Biology and Physiology Center, National Heart, Lung and Blood Institute, National Institutes of Health, Bethesda, Maryland 20892

[2]Howard Hughes Medical Institute, Janelia Research Campus, Ashburn, Virginia 20147

[3]Laboratory of Molecular Cardiology, National Heart, Lung and Blood Institute, National Institutes of Health, Bethesda, Maryland 20892

Abstract

Cellular mechanisms governing non-muscle myosin 2 (NM2) filament assembly are largely unknown. Using EGFP-NM2A knock-in fibroblasts and multiple super-resolution imaging modalities, we characterized and quantified the sequential amplification of NM2 filaments within lamella, wherein filaments emanating from single nucleation events continuously partition, forming filament clusters that populate large-scale actomyosin structures deeper in the cell. Individual partitioning events coincide spatially and temporally with the movements of diverging actin fibers, suppression of which inhibits partitioning. These and other data indicate that NM2A filaments are partitioned by the dynamic movements of actin fibers to which they are bound. Finally, we showed that partition frequency and filament growth rate in the lamella depend on MLCK, and that MLCK is competing with centrally-active ROCK for a limiting pool of monomer with which to drive lamellar filament assembly. Together, our results provide new insights into the mechanism and spatio-temporal regulation of NM2 filament assembly in cells.

INTRODUCTION

Non-muscle myosin 2 (NM2) powers numerous fundamental processes at the cellular, tissue, and organismal levels[1, 2]. A monomer of NM2 consists of two non-muscle myosin heavy chains (MHC), two essential light chains, and two regulatory light chains (RLC). To function properly, upwards of 30 NM2 monomers self-assemble via electrostatic interactions between the coiled-coil portions of their MHCs to form bipolar filaments that engage and contract actin filaments of opposing polarity[3, 4]. The key mechanism regulating the concentration-dependent[5, 6] assembly of filaments is the phosphorylation of the RLC by various kinases[7], most notably myosin light chain kinase (MLCK)[8] and Rho-associated protein kinase (ROCK)[9]. This phosphorylation event drives NM2 from a folded, inactive conformation (10S) to an extended, assembly-competent conformation (6S)[5, 10–13] and accelerates NM2's actin-activated ATPase[7]. How the activation of NM2 is spatially and temporally controlled within cells to promote the assembly of region-specific actomyosin structures is largely unknown.

The lamella of polarized fibroblasts provides an excellent site in which to define the dynamics of NM2 filament assembly with high temporal and spatial resolution. A major challenge in observing filament assembly, however, lies in the fact that the length of the NM2 filament (~300 nm) is near the diffraction limit of standard light microscopy[3, 4]. Early studies using electron microscopy (EM) to circumvent this problem identified disorganized clusters of NM2 filaments in the lamella, and more organized “ribbons” or “stacks” of filaments deeper in the cytoplasm, and suggested that new filaments associated with established filaments to create both clusters and stacks[14]. Recently, Burnette and colleagues used 3D structured-illumination microscopy (3D-SIM), which provided high spatial resolution (~130 nm) with modest temporal resolution (~4 frames/min) and limited imaging duration (~3 min), to advance our understanding of NM2 filament assembly in living cells[15]. Using exogenously-expressed NM2A in U2OS osteosarcoma cells, they observed the expansion of initial NM2 filaments into the filament stacks observed previously by EM (see also Hu et al.[16] in this issue), and presented evidence consistent with this expansion being driven by the splitting of NM2 filaments.

Here we sought to extend these previous studies by quantifying NM2 filament assembly in MEFs isolated from EGFP-NM2A knock-in mice using several live-cell imaging modalities with enhanced temporal (12–30 frames/min) and spatial (100–140 nm) resolution[17, 18], and extended imaging duration (up to 90 min). We show that NM2A filament assembly in the lamella is driven by sequential amplification in which filaments are continuously partitioned by dynamic actin fibers to which they are bound, that the NM2 filament clusters created by sequential amplification feed large actomyosin structures deeper in the cytoplasm, and that two major RLC kinases are competing for a limiting pool of myosin monomer with which to create/maintain region-specific actomyosin structures. This last observation mirrors the recent demonstration that actin nucleators compete for a limiting pool of actin monomer to create region-specific actin structures[19–22].

RESULTS

Lamellar NM2A filaments are amplified from few nucleation events by filament partitioning

To begin to define the mechanisms regulating NM2 filament assembly, we localized NM2A filaments in the lamella of primary MEFs isolated from EGFP knock-in mice, where all endogenous NM2A molecules possess EGFP at the N-terminus of their MHC[23]. 3D-SIM of cells immunostained with an isoform-specific antibody to the NM2A tail domain (Fig. 1A, magenta) yielded an alternating cyan-magenta-cyan pattern corresponding to two clusters of myosin heads at opposite ends of the ~300 nm bipolar filament (Fig. 1A, pseudocolored cyan) and a central magenta punctum identifying overlapping NM2A tails (Fig. 1A; see cartoon). Interestingly, the majority of filaments were in clusters rather than evenly dispersed in the lamella (Fig. 1A, insets A1–A6), consistent with earlier EM observations[14]. Nearest neighbor analysis demonstrated that the distance between neighbors decreases as the distance from the leading edge increases (Fig. 1B; note the negative slopes), indicating that clustering increases as filaments move further inward.

To directly observe filament nucleation, growth, and cluster formation, we turned to live-cell imaging using total internal reflection fluorescence SIM (TIRF-SIM), which provides high

spatial (~100 nm) and temporal (12 frames/min) resolution (Fig. 1C). We observed single nucleation events (Fig. 1C1–1C2; 1C1'–1C2') that expanded into filament clusters as they moved rearward (Fig. 1C3–1C6; 1C3'–1C6'; Video 1). To relate these events within the TIRF zone near the leading edge to the formation of larger actomyosin structures present deeper and higher in the cytoplasm, we performed 4D super-resolution imaging using a Zeiss 880 Airyscan confocal microscope. Depth-based pseudo-coloring of these images (Fig. 2A; Video 2) demonstrated ventral nucleation events (purple) (Fig. 2B1; 2B1') that moved rearward and upward while expanding (pink) (Fig. 2B2–B7; 2B2'–B7') to eventually populate large dorsal actomyosin structures (orange/yellow) (Fig. 2B8 and 2B8'; Video 3). Other nucleation events expanded but remained near the ventral surface and developed into ventral stress fibers (Fig. 2C; Video 4). Therefore, nucleation and expansion appears to be a major mechanism by which NM2A bipolar filaments populate both dorsal and ventral actomyosin structures (see also Hu et al.[16] for characterization of dorsal actomyosin network formation).

To define more precisely how NM2A filaments nucleate and expand, we imaged in TIRF-SIM at higher speed (30 frames/min). We observed initial nucleation events (Fig. 3A1–A2; yellow arrows) followed by a growth phase in which the intensity at each punctum increased, indicating additional monomer incorporation (Fig. 3A3–A6). Subsequently, we observed puncta at opposing ends of the mature filament partition to produce a second filament (Fig. 3A7–A14; blue and pink arrows; Video 5), similar to previous observations[15]. Individual partitioning events typically exhibited a progression from two head groups to three, and finally to four, although some events went directly from two to four head groups. While these images suggest that the initial filament is split in half, we refer to these events hereafter as filament partitioning because at this resolution we cannot distinguish between the splitting of an individual filament and the separation of two closely-spaced filaments. Importantly, the new filaments created by partitioning rapidly repeat this process, leading to the creation of filament clusters, as seen in Fig. 1C1'–C6'. This phenomenon was observed for ~95%of the filaments nucleated in the lamella (270 of 285 nucleation events from 14 cells). Notably, we observed similar filament partitioning in COS7 cells expressing EGFP-NM2B (Fig. S2A: Video 6) and in *Drosophila melanogaster* cells expressing GFP-squash (*Dm* NM2 RLC) (Fig. S2C–S2F; Video7), suggesting evolutionary conservation. Additionally, we identified nascent filaments and filament clusters containing both NM2A and NM2B in EGFP-NM2A MEFs expressing Halo-Janelia Fluor 549-NM2B (Fig. S2B; Video 8), suggesting partitioning of heterotypic filaments[17, 24].

To rule out the possibility that the "new" filaments created by partitioning are actually preexisting filaments that moved axially into the TIRF zone, we collected Airyscan z-stacks through the entire lamellum to analyze orthogonal views of partitioning events (Fig. 3B–D; Video9). The partitioning events imaged in this manner occurred laterally and did not involve the axial movement of pre-existing filaments into the image plane. Furthermore, the intensity of the two new puncta immediately following a partitioning event dropped to a mean of ~60% of the single punctum just prior to separation (Fig. 3E), consistent with a single group of NM2A molecules partitioning into two groups of NM2A molecules, along with continued filament growth throughout the process. Of note, many of these partitioning events were not even, with one punctum possessing significantly more signal than the other.

Moreover, we did not observe a consistent intensity at which partitioning occurs (Fig. 3F and 3G and Video10), arguing that filaments do not partition at a discrete size. This data must be interpreted cautiously, however, because at SIM resolution a single head punctum could contain the ends of more than one filament. Together, these data indicate that NM2A filament formation in polarized fibroblasts involves an amplification process in which filaments are sequentially partitioned to produce many filaments.

Actin filament motion drives NM2 filament partitioning

We performed several experiments to determine if the movements of actin fibers drive filament partitioning. First, we used two-color Airyscan imaging to determine if filament partitioning events correlate in space and time with the dynamic movements of F-actin, which is both dense and dynamic in the lamella (Video 11), creating myriad opportunities for actin-assisted NM2A filament partitioning. Fig. 4 shows an example of an EGFP-NM2A filament (fire LUT) that nucleated along an actin fiber (grey) (Fig. 4A1), grew (Fig. 4A2), and then partitioned (Fig. 4A3–A5; separating head clusters demarcated by white and cyan arrows; separating actin filaments outlined with dotted yellow line; Video 12; second example in Video 13). Importantly, the partitioning of this filament occurred in exact temporal and spatial register with the movements of the diverging actin fibers. TIRF-SIM provided similar examples (Video 14).

Efforts to correlate filament partitioning with actin fiber dynamics quantitatively were hampered by the high density of lamellar F-actin. Therefore, we employed fixed-cell analyses to correlate the positions of partitioning NM2 filaments with the positions of associated actin fibers. Mid-partition events, defined as three EGFP puncta (magenta) trifurcated by a single α-NM2A tail punctum (cyan) in 3D-SIM images (Fig. 4B and 4C1), were first identified in fixed, phalloidin-stained EGFP-NM2A MEFs immunostained with NM2A tail antibody as in Fig. 1A. Using 3D reconstructions of NM2A and actin, we found that the two separated NM2 head groups (“b” and “c”) had significantly more of their surface in contact with an actin surface than in randomized controls, arguing that these head groups were associated intimately with actin fibers (Fig. 4C4 and 4D; see Fig. S3A–S3H for details). Importantly, ~80% (38 of 47 events) of separated head groups appeared to be bound to different actin fibers (e.g. Fig. 4C1–C3). This quantitative analysis provided strong support for our conclusion that actin fiber dynamics actively partition NM2A filaments.

We next sought to determine if reducing actin dynamics would reduce the frequency of filament partitioning events and the total amount of NM2A per filament cluster. Actin dynamics in the lamella are driven largely by formin- and Arp2/3-dependent actin nucleation and NM2-dependent contractile forces[25,26]. We used the pan-formin inhibitor SMIFH2 and the Arp2/3 inhibitor CK666 at 5 μM each, which effectively stalled actin dynamics (Video 15) without inducing cell retraction. We then used TIRF-SIM to track the number of maxima (i.e. NM2A head groups) (Fig. S3I; Video 16) as a measure of partitioning frequency, and Airyscan imaging to track total filament intensity (Fig. S3J) as a measure of filament cluster growth rate. Fig. 4E and 4F show that the combinatorial inhibition of formins and Arp2/3 significantly reduced both rates, arguing that the sequential amplification of NM2A filaments is driven at least partially by dynamic actin.

MLCK drives filament assembly in the lamella and competes with ROCK for limiting NM2 monomer

MLCK and ROCK are the dominant NM2 RLC kinases in most cells, with MLCK being primarily responsible for RLC phosphorylation and filament assembly in the lamella[27, 28] and ROCK being primarily responsible for these events in central and posterior regions, where it drives stress fiber formation[28, 29]. We used small-molecule inhibitors of ROCK (Y27632) and MLCK (ML7) to define their roles in NM2 filament assembly and partitioning. ROCK inhibition resulted in the rapid and dramatic redistribution of EGFP-NM2A from central and posterior stress fibers to the lamella (Fig. 5A; Video 17), which was reversible upon washout (Fig. S4). This dramatic increase in lamellar EGFP signal following ROCK inhibition was due to a large increase in the number of NM2 filaments present there and not simply to an increase in signal from NM2 monomer (Fig. 5B–D). Moreover, quantitative live-cell imaging revealed that this increase in filament number coincided with significant increases in the rates of both filament partitioning and filament cluster growth (Fig. 5E and 5F, magenta lines; TIRF-SIM examples in 5G and 5H). As anticipated, inhibition of MLCK in EGFP-NM2A MEFs resulted in significant decreases in the rates of both filament partitioning and filament cluster growth in lamella (Fig. 5E and 5F, green lines; TIRF-SIM example in 5I). Importantly, simultaneously inhibiting MLCK and ROCK resulted in complete suppression of the Y27632-induced enhancement of filament partitioning in the lamella, and partial suppression of the Y27632-induced enhancement of lamellar filament cluster growth (Fig. 5E and 5F, cyan lines; TIRF-SIM example in 5J). Together, these results demonstrate that MLCK plays a major role in the sequential amplification of NM2 filaments in the lamella, and suggest a more complex interplay between ROCK and MLCK than previously appreciated.

A straightforward way to explain the rapid, MLCK-dependent increase in lamellar NM2A filament assembly following the Y27632-induced stress fiber disassembly is to assume that the amount of NM2 monomer available for filament assembly at steady-state is limiting, such that the size of this monomer pool increases significantly following stress fiber disassembly. Implicit in this explanation is the idea that spatially-restricted RLC kinases are competing for a pool of NM2 monomer that is limiting for filament assembly. To further explore this hypothesis, we artificially altered NM2A levels. To lower expression, we used a partial knockdown to reduce NM2A levels to ~50% of wild-type (Fig. 6A, cyan), measured using the EGFP signal and FACS (further reduction in NM2A expression altered cell morphology, prohibiting analysis). Consistent with limiting NM2 monomer, this moderate reduction in NM2A level reduced significantly the rates of both filament partitioning and cluster growth in the lamella (Fig. 6B and 6C, cyan lines). To increase expression, we transiently expressed NM2A tagged with EGFP and mApple and used FACs to purify a population of cells with ~2-fold more NM2A than control cells (i.e. mApple-positive cells with ~2 fold more EGFP signal) (Fig. 6A, magenta). Consistent with limiting NM2 monomer, these over-expressing cells displayed significantly enhanced rates of filament partitioning and cluster growth in the lamella (Fig. 6B and 6C, magenta lines). Finally, under-expressing cells treated with Y27632 displayed significantly reduced rates of filament partitioning and cluster growth relative to Y27632-treated normal-expressing cells (Fig. 6D and 6E, cyan lines), consistent with the data for untreated cells. Interestingly, while filament

partitioning and cluster growth trended towards higher values in over-expressing cells treated with Y27632, the rates were not statistically different from normal-expressing cells treated with Y27632, suggesting monomer concentrations are approaching saturating levels following stress fiber disassembly. Together, these data argue that the level of NM2A monomer available for RLC kinase-dependent filament assembly at steady state is limiting, such that the kinases compete for this limiting pool of monomer.

DISCUSSION

Using several super-resolution imaging modalities with enhanced speed and extended imaging duration, we showed here that NM2 filament assembly in the lamella of EGFP-NM2A knock-in MEFs occurs via sequential amplification following initial nucleation, where relatively sparse nucleation events give rise to filament clusters that then populate large-scale actomyosin structures present deeper in the cell. Fast TIRF-SIM imaging was particularly effective in revealing the filament partitioning events that rapidly transform nascent filaments into large filament clusters via sequential amplification. This, combined with Airyscan imaging and 3D-SIM, allowed us to quantitate both partitioning frequency and the growth rate of filament clusters, and to correlate filament partitioning with diverging actin fibers. Finally, by quantitating regional filament assembly parameters following inhibition of MLCK and ROCK, we showed that these kinases are competing for limiting NM2 monomer, and we provided evidence that filaments assembled in the lamella downstream of MLCK populate stress fibers that are maintained by ROCK. Together, our results confirm and significantly extend those of Fenix et al. in U2OS cells over-expressing GFP-NM2A, who also saw filament partitioning and then examined the phenomena of filament stack formation.

With regard to what is actually occurring during filament partitioning, two obvious possibilities come to mind. In the first, which we term templated-nucleation, a parent filament assists the nucleation of a new, immediately adjacent filament. In this case, therefore, the parent filament does not split into two daughters but rather gives birth to a daughter (Fig. S5A). Even with the spatial resolution SIM provides, this daughter filament would remain unresolvable until it moved a sufficient distance away from the parent filament. In the second possibility, the parent filament actually "splits" into two daughter filaments (Fig. S5B). This model, similar to one proposed by Fenix et al.[15], seems less likely given that the electrostatic forces holding individual filaments together are probably quite high. That said, bundles of myosin molecules can be mechanically “unzipped” from thick filaments with relatively moderate forces[30], and filament stability may be more easily compromised by lateral forces applied perpendicular to the filament’s long axis, as seen in the actin-assisted filament partitioning described here, than by forces parallel to their long axis, as seen in normal sarcomeric arrangements. Nevertheless, we tend to favor the templated-nucleation model for energetic reasons and because the inter-filament connections inherent in it could provide the kinetic advantage driving templated-nucleation (see below). Ultimately, correlative EM, light-based molecule counting methods, and reconciliation with current NM2 filament assembly models[31–33]will be required to fully understand the partitioning process.

While we have no definitive answer for why NM2 filament proliferation occurs via sequential amplification rather than widespread *de novo* nucleation, two factors might promote sequential amplification. The first stems from the templated-nucleation model described above. If filament nucleation is faster when seeded off of an existing filament than when nucleated in isolation, then sequential amplification would have a competitive advantage. The second stems from our demonstration that NM2 monomer levels are limiting, and the likelihood that the monomer concentration required to promote templated-nucleation is lower than that required to promote *de novo* nucleation. Importantly, the magnitude of this advantage would grow as monomer is consumed. The common consequence of these two factors would be positive cooperativity that provides sequential amplification with a strong competitive advantage over *de novo* nucleation.

A major mechanistic conclusion from our work is that filaments are partitioned by the dynamics of actin fibers to which they are bound. This conclusion was based on dynamic, two-color, super-resolution imaging demonstrating that NM2A filaments partition in spatial and temporal register with diverging actin fibers, 3D-SIM images of mid-partitioning events showing that the majority of separating NM2A head groups are bound to different actin fibers, and evidence that inhibiting actin dynamics suppresses filament partitioning and filament cluster growth, consistent with previous end-point images of cytochalasin-treated cells[15]. Importantly, diverging actin fibers could drive either the separation of a templated filament from the parent filament or the splitting of a single filament whose heads bridge the diverging fibers (Fig. S5). Moreover, the actin-dependent partitioning of NM2 filaments might function in a feedforward fashion to promote the formation of macro-scale actomyosin networks (Fig. S6), which, together with the work of Hu and colleagues[16], adds new layers of complexity to previous studies demonstrating actin-facilitated NM2 assembly[34–36] and the mechano-accumulative properties of NM2[33, 37].

A final major mechanistic conclusion from our work is that spatially-restricted RLC kinases are competing for alimiting pool of NM2 monomer. Competition occurs when two (or more) enzymes are simultaneously using the same diffusible substrate, and this substrate is present at sub-saturating/limiting concentrations. Two key observations support our conclusion regarding monomer competition. First, MLCK-dependent filament assembly in the lamella increases following either stress fiber disassembly downstream of ROCK inhibition or an elevation in NM2A expression level. These results indicate that the level of NM2A monomer at steady state is limiting, not saturating. Second, selective inhibition of MLCK and ROCK showed that both are continuously driving filament assembly, i.e. both are simultaneously active. Recent paradigm-shifting studies in yeast and vertebrate cells have demonstrated that formins and the Arp2/3 complex compete for a limiting pool of actin monomer, such that when one nucleating machine is turned off, the filaments created by the other machine proliferate[19–22]. Similarly, our results suggest that enhanced NM2 filament assembly within a particular area could be driven not only by direct activation of the RLC kinase serving that area but by inactivation of competing RLC kinases elsewhere. This conclusion raises interesting possibilities for unrecognized crosstalk between upstream signaling pathways in processes involving large rearrangements of actomyosin, such as cytokinesis and EMT.

METHODS

Cell isolation, culture and transfection

MEFs were isolated from EGFP-NM2A knock-in mice[23] as previously described[38] and used within 5 passages. Cells were grown in Dulbecco's modified Eagle's medium supplemented with 10% fetal bovine serum, 2 mM GlutaMAX (Life Technologies, Grand Island, NY), and 1X antibiotic-antimycotic (Life Technologies), and maintained at 37°C in 5% CO2. All coverslips were coated with 10 μg/ml fibronectin (Sigma, St. Louis, MO) prior to use. Cells were transferred to Leibovitz's L-15 medium supplemented with 10% fetal bovine serum during live-cell imaging. Cells were transfected using a Lonza Nucleofector system with a solution of 5 mM KCl, 15 mM $MgCl_2$, 120 mM Na_2HPO_4/NaH_2PO_4, pH 7.2, 50 mM mannitol and program A-24 for MEFs and W-01 for COS-7. For over-expression studies, EGFP-NM2A MEFs were transfected with pEGFP-NM2A-mApple as described above. At ~24 hours post-transfection, the brightest half of the mApple-positive population was isolated using a BD FACS Aria Flow Cytometer. For knockdown studies, EGFP-NM2A MEFs were transduced with Myh9 shRNA from the Broad Institute's Mission TRC-1 mouse library (TRCN0000071506: target sequence 5'-GCCATACAACAAATACCGCTT-3'). At 12 hrs post-transduction, the cells were grown for 24 hrs in 10 μg/ml puromycin and then plated for imaging. The following inhibitors were purchased from Sigma-Aldrich and used at the indicated concentration: Y27632, 10 μm; ML7, 20 μm; SMIFH2, 5 μm; CK666, 5 μm. *Drosophila melanogaster* cells were cultured from transgenic animals ubiquitously over-expressing spaghetti squash tagged with GFP. Cells were isolated from pre-pupae by puncturing the cuticle slightly anterior to the posterior spiracles with a 27 gauge needle, allowing the haemolymph to bleed into Schneider's *Drosophila* Media supplemented with 20% FBS. Cells were plated on an uncoated coverslip and imaged within ~1 hr of plating. None of the cell lines used in the study are on the list of misidentified cell lines maintained by ICLAC and NCBI biosample. COS-7 cell lines were not authenticated and were not tested for mycoplasma contamination.

Antibodies and immunofluorescence

Cells were fixed in a solution containing 4% formaldehyde, 150 mM NaCl, 5 mM EGTA, 5 mM glucose, 5 mM MgCl2, and 10 mM PIPES (pH 6.8). Cells were simultaneously permeabilized and blocked in 1×PBS containing 0.2% Saponin and 5% normal goat serum. Primary and secondary antibody incubations were performed for 2 hrs at room temperature in permeabilization/blocking solution. The rabbit polyclonal antibody against non-muscle MHC 2A was purchased from Sigma (#M8064) and used at a 1:500 dilution, while the mouse monoclonal antibody against GFP was purchased from Roche (#11814460001) and used at a 1:2000 dilution. AlexaFluor-conjugated secondary antibodies and phalloidin were purchased from Life Technologies. Cells were incubated with phalloidin (1:200) in permeabilization/blocking solution overnight at 4°C.

Expression vectors

Plasmid EGFP-NM2A-mApple was created by combining pEGFP-C3-NM2A with pmApple-N1-NM2A using an upstream Nhe1 site and an internal EcoR1 site in the NM2A coding sequence (Nhe1-EGFP-NM2A-EcoR1 transferred into pmApple-N1-NM2A

backbone). Plasmid mApple-F-Tractin was described previously[17]. Plasmid tdTomato-F-Tractin was created by replacing mApple with tdTomato using restriction enzymes Age1 and BsrG1. pEGFP-NM2B was a gift of Dr. Tom Egelhoff (CCF). pHalo-N1-NM2B was created by PCR amplifying the Halo-tag coding sequence and cloning it into pmApple-N1-NM2B using In-Fusion HD Cloning (Takara) following removal of the mApple fluorophore with Age1/Not1 digestion. Janelia Fluor 549 (JF549) Halo Tag ligand was a gift from Luke Lavis (Janelia Research Campus).

Imaging

TIRF-SIM imaging was performed on either a custom TIRF-SIM microscope at the Janelia Research Campus as previously described[17] or a DeltaVision OMX SR (GE) microscope equipped with a 60× 1.42 NA objective. All 2D- and 3D-SIM imaging was performed on a DeltaVision OMX 3D-SIM Imaging System V4 (GE) equipped with an Olympus 60×/1.42 NA objective. Raw images were reconstructed using Softworx (Applied Precision). For 2D-SIM, a Weiner constant of 0.2 was used for every frame of processing. For 3D-SIM, a Weiner constant of 0.001 was used. Processed SIM images were zero-clipped to remove negative pixel values. Of note, some SIM images contain faint horizontal “stripes” that arise when imaging near the lower end of the CMOS camera’s dynamic range. Airyscan imaging was performed in Superresolution mode on a Zeiss LSM 880 Airyscan microscope equipped with a 63× 1.4 NA objective. Raw data was processed using Airyscan processing in “auto strength” mode (mean strength +/− S.D. = 5.5+/− 1.3) with Zen Black software version 2.3. Fig. 5A was collected on a Nikon A1R microscope equipped with a 40× 1.3 NA objective. Linear adjustments for contrast and brightness were made to images using ImageJ.

Measuring partitioning rate and filament cluster growth rate

Individual NM2A filament clusters in the lamella that did not overlap with other clusters within 3 minutes of nucleation were selected from the whole-cell image for analysis. These filament clusters were traced backwards in time to their nucleation point. TIRF-SIM images were used for maxima tracking to obtain filament partitioning rates. Maxima were identified using “Find maxima…” in ImageJ. Airyscan images were used to measure filament cluster growth rates. A mask was created at each time point using ImageJ auto threshold, which was then applied to the raw image to find the area and mean EGFP intensity. These data were multiplied to calculate total intensity for each filament cluster at each time point. See examples in Figure S3. All data was graphed using GraphPad Prism. Statistical significance for both analyses was determined using a Mann-Whitney test of the best-fit slopes.

Filament counting and nearest neighbor analysis

EGFP-NM2A MEFs were stained with phalloidin-AlexaFluor633 and α-NM2A antibody to identify the tail domain of NM2, and imaged with 3D-SIM. Where indicated, the cells were treated first with small molecule inhibitors prior to fixation. Coordinates for the middle of discrete NM2A filaments were manually identified from the alternating head-tail-head pattern (see cartoon in Fig. 1A). Of note, filaments that were not clearly discernable were not counted. Coordinates for the leading edge were identified by manually tracing the leading edge using the actin channel. Distances between filaments and the leading edge or between filaments and other filaments (for nearest neighbor analysis) was calculated in

Excel. All data was graphed using GraphPad Prism. Statistical significance was determined using an unpaired t-test with Welch's correction.

Measuring partitioning head puncta intensities

To track filament intensity throughout individual partitioning events (Fig. 3E), EGFP-NM2A MEFs were imaged with TIRF-SIM. Puncta that exhibited a clear and discrete partitioning event (i.e. from one punctum to two puncta) over 1–2 frames were analyzed. To determine if there was a consistent head puncta intensity at which partitioning events occurred (Fig. 3F and 3G), EGFP-NM2A MEFs were imaged with wide-field 2D-SIM to circumvent intensity changes caused by variations in z that are inherent in TIRF imaging. For each data set, a mask was created in Image J for each EGFP punctum, which was then applied to the raw image to find the area and mean EGFP intensity. These data were multiplied to calculate total intensity for each punctum. For Fig. 3E this was done at each time point and data were normalized to the maximum intensity, which was the last time point just prior to the partitioning event. For Fig. 3F, puncta were measured at the time point immediately preceding partitioning. Data was graphed using GraphPad Prism.

Surface-surface contact

EGFP-NM2A MEFs stained with phalloidin-AlexaFluor568 and immunostained with α-NM2A and α-GFP were imaged with 3D-SIM. From 40 cells, 47 NM2A trimers were selected based on having three distinct EFGP- NM2A head puncta trifurcated by a single α-NM2A heavy chain punctum to identify the tail (see cartoon in Figure 4B). Each trimer was extracted as a 1 μM z-stack and imported into Imaris 3D visualization software (Biplane) and 4 different channels were analyzed: NM2A head clusters, actin, and two different areas of control actin. The controls were regions of actin adjacent to the ROI that had similar actin density. Using Imaris software, the "Surfaces" tool was used to create a 3D rendering of each channel (as in Figure 4C1–C3). Using these rendered surfaces, a surface-surface contact area algorithm was used to determine the amount of contact between the NM2A surface and the actin surface (Figure 4C4). This algorithm creates a 1 voxel shell around the primary surface (NM2A) and calculates the percentage of that shell that overlaps with the secondary surface (actin). This same calculation was done with the random controls. These surfaces were also used to determine whether the splitting NM2A head clusters ("b" and "c" in Fig. 4B) were attached to the same or different actin fiber. Of the 47 mid-partitioning events analyzed, 38 of the separated head clusters were definitively on different actin filaments/bundles, 4 were inconclusive, and 5 appeared attached to the same actin filament/bundle. All data was graphed using GraphPad Prism. The surface-surface contact method is further explained in Figure S3A–S3H. Statistical significance of the contact data (Figure 4D) was determined using an unpaired t-test with Welch's correction.

Statistics and reproducibility

The type of statistical test, n values, and p values are all listed in the figure legends. All statistical analyses were performed using Graph Pad Prism, and significance was determined using a 95% confidence interval. The number of cells examined and experimental repeats not indicated in the legend or text are as follows: Fig. 1B, filaments analyzed in 9 cells acquired in 4 independent experiments; Fig. 3E, partitioning events analyzed in 6 cells

acquired in 6 independent experiments; Fig. 3F, head puncta during partitioning analyzed in 22 cells acquired in 3 independent experiments; Fig. 4D, filaments analyzed in 40 cells acquired in 2 independent experiments; Fig. 4F, filaments pre/and post SMIFH2/CK666 treatment analyzed in 5 cells acquired in 3 independent experiments; Fig. 5D, cells acquired in 5 experiments (Untreated) or 3 experiments (Y27632). For Figs. 4E, 5E, 6B, 6D, the number of cells examined and experimental repeats for each subgroup, which could be shown in multiple figures, were as follows: Untreated (13, 5), + SMIFH2/CK666 (9, 3), + Y27632 (15,4), + ML7 (10,3), + Y27632/ML7 (11,3), EGFP-NM2A-mApple (8,2), NM2A shRNA (9,2), EGFP-NM2A-mApple + Y27632 (8,2), NM2A shRNA + Y27632 (5,2). For Figs. 5F, 6C, 6E, these values were: Untreated (8, 4), + Y27632 (5,3), + ML7 (5,3), + Y27632/ML7 (6,2), EGFP-NM2A-mApple (7,2), NM2A shRNA (6,2), EGFP-NM2A-mApple + Y27632 (7,2), NM2A shRNA + Y27632 (5,2). For Fig. 6A, these values were: C57B6 wild-type and NM2A shRNA (3 experiments), Untreated (6 experiments), and EGFP-NM2A-mApple (4 experiments).

Data Availability

All primary data supporting the conclusions made is available from the authors upon request.

Supplementary Material

Refer to Web version on PubMed Central for supplementary material.

Acknowledgments

The authors thank Xufeng Wu, Jim Sellers, Sarah Heissler, Neil Billington, Ana Pasapera, Michelle Baird, Vinay Swaminathan, Lois Greene, Evan Eisenberg, Andrew Doyle, Tom Egelhoff, Luke Lavis, Matthew Gastinger, the NHLBI Flow Cytometry Core, and GE Deltavision for reagents, help with data acquisition and analysis, critical reading of the manuscript, and helpful discussions.

Reference List

1. Heissler SM, Manstein DJ. Nonmuscle myosin-2: mix and match. Cell Mol Life Sci. 2013; 70:1–21. [PubMed: 22565821]
2. Ma X, Adelstein RS. The role of vertebrate nonmuscle Myosin II in development and human disease. Bioarchitecture. 2014; 4:88–102. [PubMed: 25098841]
3. Billington N, Wang A, Mao J, Adelstein RS, Sellers JR. Characterization of three full-length human nonmuscle myosin II paralogs. J Biol Chem. 2013; 288:33398–33410. [PubMed: 24072716]
4. Niederman R, Pollard TD. Human platelet myosin. II. In vitro assembly and structure of myosin filaments. J Cell Biol. 1975; 67:72–92. [PubMed: 240861]
5. Kendrick-Jones J, Smith RC, Craig R, Citi S. Polymerization of vertebrate non-muscle and smooth muscle myosins. J Mol Biol. 1987; 198:241–252. [PubMed: 3430607]
6. Pollard TD. Structure and polymerization of Acanthamoeba myosin-II filaments. J Cell Biol. 1982; 95:816–825. [PubMed: 7153247]
7. Adelstein RS, Conti MA. Phosphorylation of platelet myosin increases actin-activated myosin ATPase activity. Nature. 1975; 256:597–598. [PubMed: 170529]
8. Daniel JL, Adelstein RS. Isolation and properties of platelet myosin light chain kinase. Biochemistry. 1976; 15:2370–2377. [PubMed: 132187]
9. Amano M, et al. Phosphorylation and activation of myosin by Rho-associated kinase (Rho-kinase). J Biol Chem. 1996; 271:20246–20249. [PubMed: 8702756]

10. Craig R, Smith R, Kendrick-Jones J. Light-chain phosphorylation controls the conformation of vertebrate non-muscle and smooth muscle myosin molecules. Nature. 1983; 302:436–439. [PubMed: 6687627]
11. Scholey JM, Taylor KA, Kendrick-Jones J. Regulation of non-muscle myosin assembly by calmodulin-dependent light chain kinase. Nature. 1980; 287:233–235. [PubMed: 6893621]
12. Trybus KM, Huiatt TW, Lowey S. A bent monomeric conformation of myosin from smooth muscle. Proc Natl Acad Sci U S A. 1982; 79:6151–6155. [PubMed: 6959106]
13. Suzuki H, Onishi H, Takahashi K, Watanabe S. Structure and function of chicken gizzard myosin. J Biochem. 1978; 84:1529–1542. [PubMed: 153905]
14. Verkhovsky AB, Svitkina TM, Borisy GG. Myosin II filament assemblies in the active lamella of fibroblasts: their morphogenesis and role in the formation of actin filament bundles. J Cell Biol. 1995; 131:989–1002. [PubMed: 7490299]
15. Fenix AM, et al. Expansion and concatenation of non-muscle myosin IIA filaments drive cellular contractile system formation during interphase and mitosis. Mol Biol Cell. 2016
16. Shiqiong, Hu, et al. Long range self-organization of cytoskeletal myosin-II filament stacks. Nat. Cell Biol. 2016
17. Beach JR, et al. Nonmuscle myosin II isoforms coassemble in living cells. Curr. Biol. 2014; 24:1160–1166. [PubMed: 24814144]
18. Li D, et al. ADVANCED IMAGING. Extended-resolution structured illumination imaging of endocytic and cytoskeletal dynamics. Science. 2015; 349:aab3500. [PubMed: 26315442]
19. Suarez C, et al. Profilin regulates F-actin network homeostasis by favoring formin over Arp2/3 complex. Dev Cell. 2015; 32:43–53. [PubMed: 25543282]
20. Rotty JD, et al. Profilin-1 serves as a gatekeeper for actin assembly by Arp2/3-dependent and -independent pathways. Dev Cell. 2015; 32:54–67. [PubMed: 25543281]
21. Suarez C, Kovar DR. Internetwork competition for monomers governs actin cytoskeleton organization. Nat Rev Mol Cell Biol. 2016; 17:799–810. [PubMed: 27625321]
22. Murugesan S, et al. Formin-generated actomyosin arcs propel T cell receptor microcluster movement at the immune synapse. J Cell Biol. 2016; 215:383–399. [PubMed: 27799367]
23. Zhang Y, et al. Mouse models of MYH9-related disease: mutations in nonmuscle myosin II-A. Blood. 2012; 119:238–250. [PubMed: 21908426]
24. Shutova MS, Spessott WA, Giraudo CG, Svitkina T. Endogenous species of mammalian nonmuscle myosin IIA and IIB include activated monomers and heteropolymers. Curr. Biol. 2014; 24:1958–1968. [PubMed: 25131674]
25. Guo M, et al. Probing the stochastic, motor-driven properties of the cytoplasm using force spectrum microscopy. Cell. 2014; 158:822–832. [PubMed: 25126787]
26. Comrie WA, Babich A, Burkhardt JK. F-actin flow drives affinity maturation and spatial organization of LFA-1 at the immunological synapse. J Cell Biol. 2015; 208:475–491. [PubMed: 25666810]
27. Chew TL, Wolf WA, Gallagher PJ, Matsumura F, Chisholm RL. A fluorescent resonant energy transfer-based biosensor reveals transient and regional myosin light chain kinase activation in lamella and cleavage furrows. J Cell Biol. 2002; 156:543–553. [PubMed: 11815633]
28. Totsukawa G, et al. Distinct roles of ROCK (Rho-kinase) and MLCK in spatial regulation of MLC phosphorylation for assembly of stress fibers and focal adhesions in 3T3 fibroblasts. J Cell Biol. 2000; 150:797–806. [PubMed: 10953004]
29. Newell-Litwa KA, et al. ROCK1 and 2 differentially regulate actomyosin organization to drive cell and synaptic polarity. J Cell Biol. 2015; 210:225–242. [PubMed: 26169356]
30. Decker B, Kellermayer MS. Periodically arranged interactions within the myosin filament backbone revealed by mechanical unzipping. J Mol Biol. 2008; 377:307–310. [PubMed: 18262203]
31. Sinard JH, Stafford WF, Pollard TD. The mechanism of assembly of Acanthamoeba myosin-II minifilaments: minifilaments assemble by three successive dimerization steps. J Cell Biol. 1989; 109:1537–1547. [PubMed: 2793933]

32. Sinard JH, Pollard TD. Acanthamoeba myosin-II minifilaments assemble on a millisecond time scale with rate constants greater than those expected for a diffusion limited reaction. J Biol Chem. 1990; 265:3654–3660. [PubMed: 2303471]

33. Luo T, et al. Understanding the cooperative interaction between myosin II and actin cross-linkers mediated by actin filaments during mechanosensation. Biophys J. 2012; 102:238–247. [PubMed: 22339860]

34. Mahajan RK, Vaughan KT, Johns JA, Pardee JD. Actin filaments mediate Dictyostelium myosin assembly in vitro. Proc Natl Acad Sci U S A. 1989; 86:6161–6165. [PubMed: 2762319]

35. Applegate D, Pardee JD. Actin-facilitated assembly of smooth muscle myosin induces formation of actomyosin fibrils. J Cell Biol. 1992; 117:1223–1230. [PubMed: 1607384]

36. Mahajan RK, Pardee JD. Assembly mechanism of Dictyostelium myosin II: regulation by K+, Mg2+, and actin filaments. Biochemistry. 1996; 35:15504–15514. [PubMed: 8952504]

37. Ren Y, et al. Mechanosensing through cooperative interactions between myosin II and the actin crosslinker cortexillin I. Curr. Biol. 2009; 19:1421–1428. [PubMed: 19646871]

Reference List

38. Bockholt SM, Burridge K. An examination of focal adhesion formation and tyrosine phosphorylation in fibroblasts isolated from src-, fyn-, and yes- mice. Cell Adhes. Commun. 1995; 3:91–100. [PubMed: 7583009]

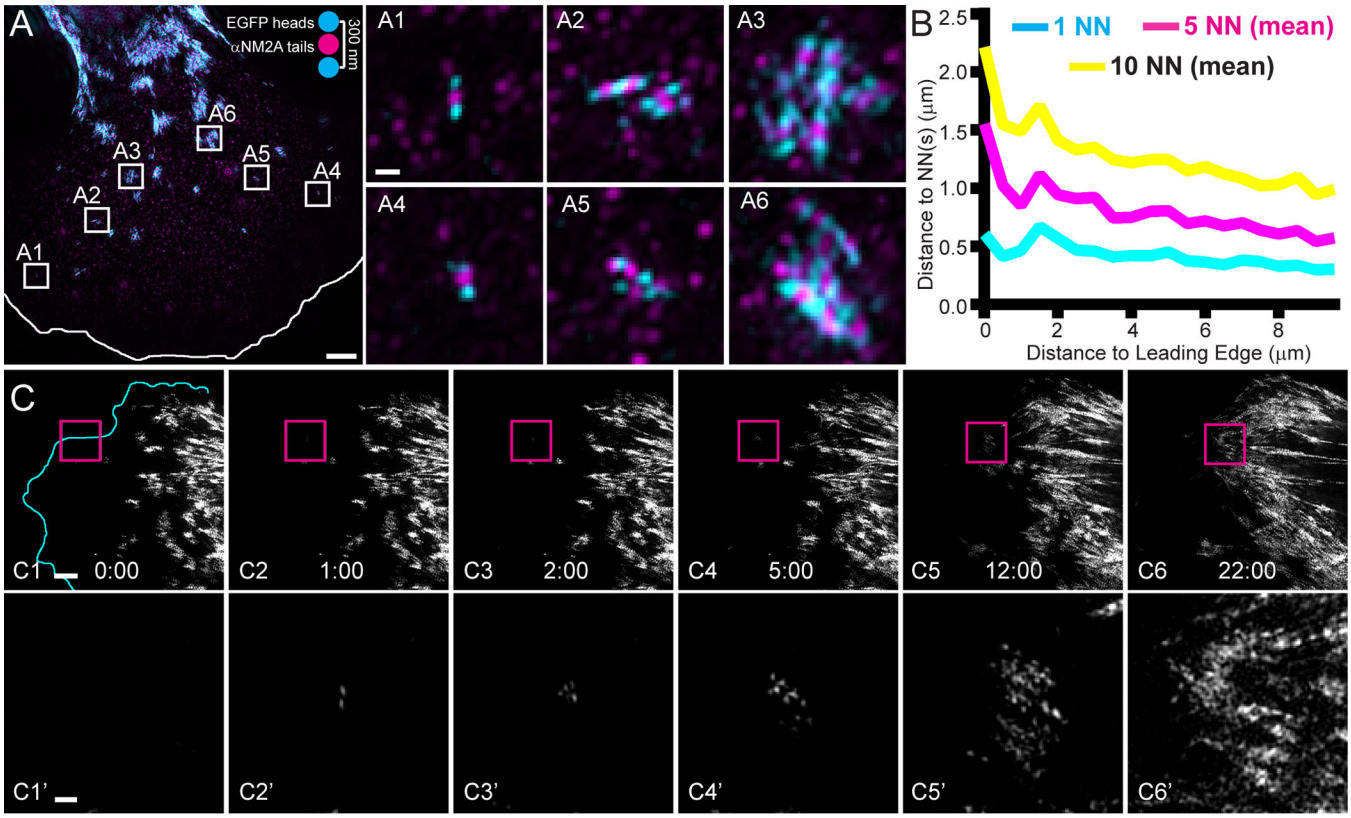

Figure 1. NM2A filament clusters are derived from single nucleation events

A) EGFP-NM2A MEFs (cyan) were fixed, immunostained with αNM2A (magenta), and imaged with 3D-SIM. Image is a mean z-projection. EGFP-NM2A filaments appear as alternating cyan-magenta-cyan with cyan puncta ~300 nm apart (see cartoon inset). White line indicates leading edge. White numbered boxes correspond to the insets to the right. Scale bar represents 3 μm in A and 300 nm in A1. B) The coordinates of each filament and the leading edge were identified. The mean distances of the first nearest neighbor (NN; cyan), 5 NN (magenta), and 10 NN (yellow) were calculated and plotted as a function of distance from the leading edge. n=3523 filaments. C) EGFP-NM2A MEF sampled every 5 seconds with TIRF-SIM. Time points indicated in min:sec. Magenta boxes in C1–C6 correspond to C1'–C6' in the lower row. Scale bars represent 3 μm in C1 and 500 nm in C1'. See corresponding Video 1. Similar behavior was observed in all 13 cells imaged in this manner.

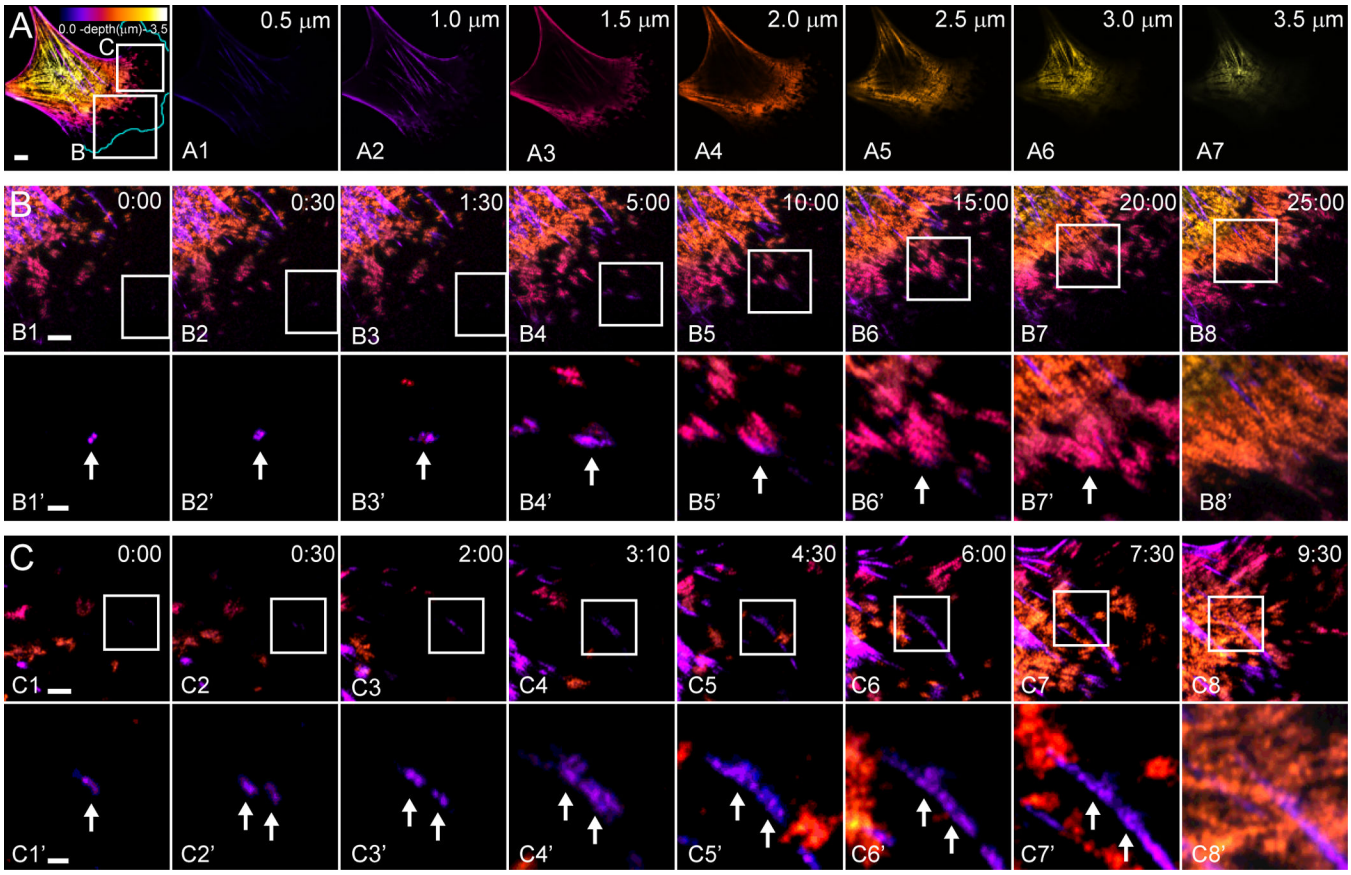

Figure 2. NM2A filament nucleation and expansion produce lamellar networks and ventral stress fibers

A) EGFP-NM2A MEF imaged with Airyscan, sampled with 0.5 μm steps every 30 seconds. Image is a maximum z-projection pseudocolored by depth (color depth scale in top right of A). A1–A8 display individual pseudocolored z-slices. Depth indicated in top right corner. Scale bar represents 5 μm. White boxes in A correspond to B and C in lower rows. B and C) Time-lapse tracking of filament clusters that moved higher in z over time (purple to pink to orange) to incorporate into lamellar networks (B) or remained in lower z planes over time (purple) to produce ventral stress fibers (C). Time points indicated in min:sec in top right corner. White boxes in B1–B8 and C1–C8 correspond to B1'–B8' and C1'–C8', respectively, in lower rows. Intensities in B1'–B8' and C1'–C8' were adjusted individually so filaments could be seen at early time points. White arrows track filament clusters over time. Scale bars represent 3 μm in B1 and C1 and 1 μm in B1' and C1'. Similar behavior was observed in all 7 cells imaged in this manner in four independent sessions. See corresponding Videos 2–4.

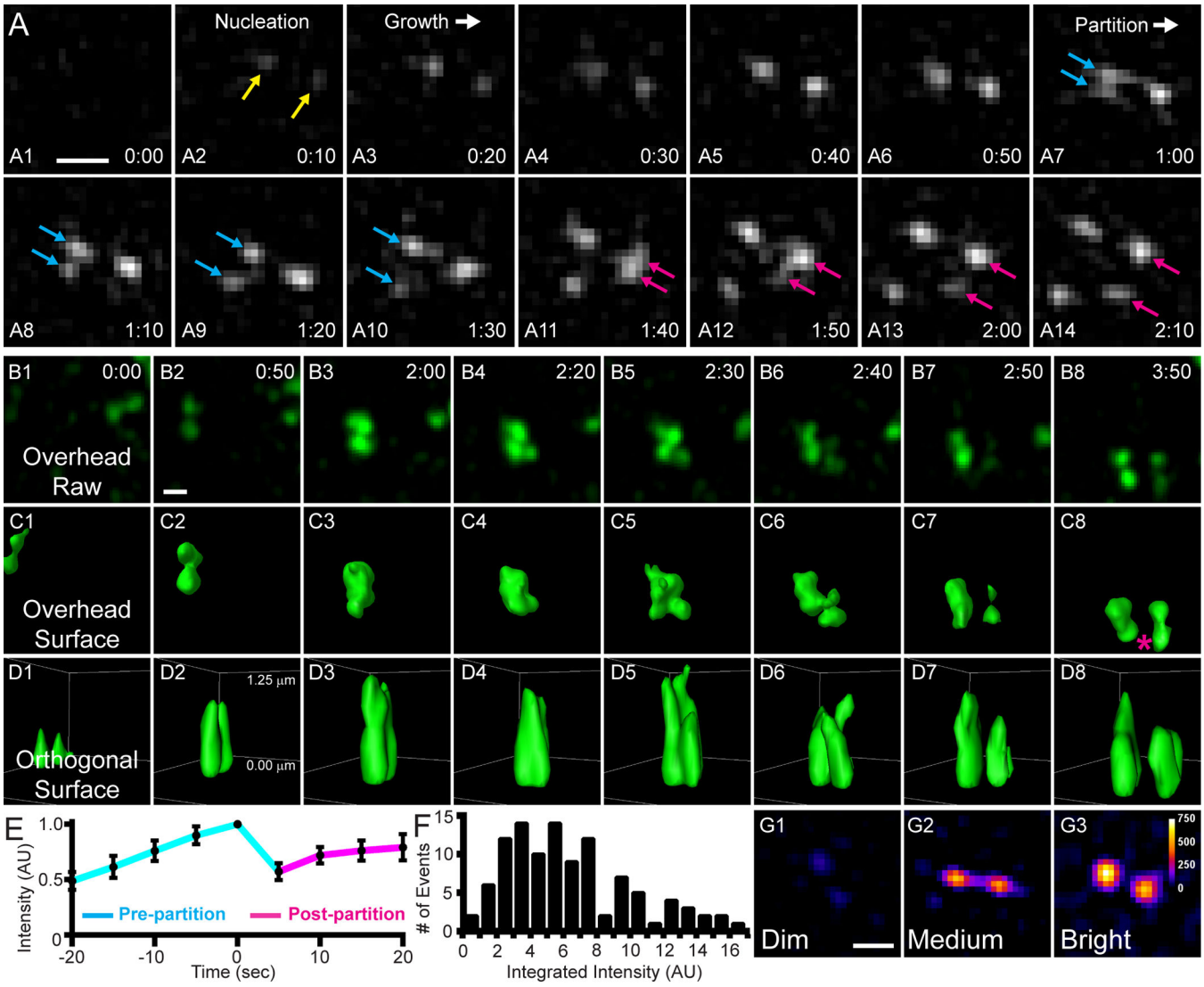

Figure 3. Partitioning of NM2A filaments

A) EGFP-NM2A MEF sampled every 2 seconds with TIRF-SIM. Time points indicated in min:sec. An EGFP-NM2A filament nucleates (A2; yellow arrows), grows (A3–A6), and partitions (A7–A14; cyan and magenta arrows indicate partitioning of NM2A head groups). B–D) Z-stacks through the entire lamella of EGFP-NM2A MEFs were acquired with Airyscan imaging every 10 seconds with 0.25 µm steps. A partition event was cropped from the lamella and rendered in 3D using Imaris software. B1–B8 display the maximum z-projection of the raw data from an overhead view. C1–C8 display surface rendering from an overhead view. D1–D8 displays the surface rendering from an orthogonal view. The orthogonal view was rotated slightly off axis for a better view down the plane of the partition event, as if the viewer was observing from slightly outside the frame near the magenta asterisk in C8. The puncta appear elongated in the orthogonal view due to the lower axial resolution (~400 nm) relative to the lateral resolution (~140 nm). Time displayed in min:sec. Top and bottom z-positions noted in D2. Note that the “new” filament partitions from the pre-existing filament and does not move into the imaging area from out of the z-plane

(consistent for all 3 filaments rendered in this manner). E) Total intensity of EGFP-NM2A puncta was tracked every 5 seconds for 20 seconds before (cyan) and after (magenta) a partitioning event. Data normalized to maximum intensity and plotted as mean +/− SEM. n=12 events. F) Measurements of EGFP intensity in head puncta just prior to partitioning. n=106 head puncta. Note that a single head punctum does not necessarily correspond to one end of a single filament, i.e. it could contain multiple filament ends. G) Three examples of EGFP-NM2A filaments just prior to partitioning pseudocolored with fire LUT. Calibration bar in upper right corner of G3 indicates intensities. All scale bars represent 300 nm. See corresponding Videos 5, 9, and 10. See Fig. S1 for larger fields of view for A–D.

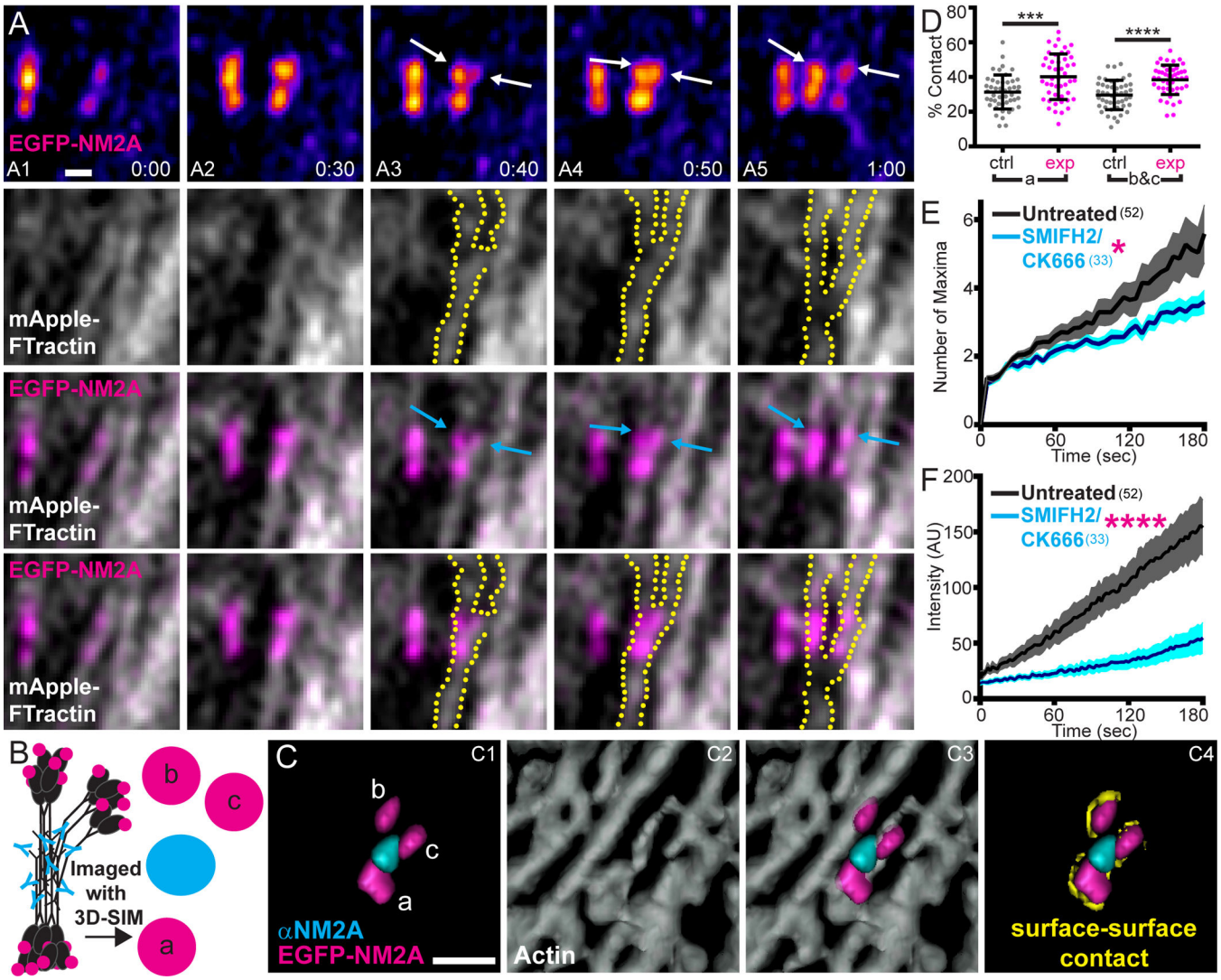

Figure 4. Actin dynamics drive partitioning

A) EGFP-NM2A MEF expressing mApple-F-Tractin imaged with Airyscan every 10 sec. EGFP-NM2A pseudocolored with fire LUT (row 1) or magenta (rows 3 and 4) and mApple-F-Tractin shown in grey scale (rows 2–4). Actin is displayed alone in row 2 and with EGFP-NM2A in rows 3 and 4. Actin fibers are outlined with yellow dots. Following nucleation and growth (A1–A2), the top head groups begin separating from each other (A3–A4; indicated by white and cyan arrows in row 1 and row 3, respectively), eventually completing the process (A5). The partitioning of the NM2A filaments coincides spatially and temporally with two diverging actin fibers (rows 2–4). Scale bar represents 300 nm. See corresponding Videos 12–14. B) Cartoon of EGFP-NM2A (magenta) filament at mid-partition immunostained with αNM2A (cyan) and imaged with 3D-SIM. Separated head groups indicated with “b” and “c” and an un-separated head group indicated with “a”. C) Representative mid-partition EGFP-NM2A filament following 3D rendering with Imaris software. Lettering of head groups corresponds to cartoon in B. Phalloidin-stained actin shown as grey scale in C2 and C3. Contact points between the EGFP-NM2A head group

surface and the actin surface were identified using a novel surface-surface contact algorithm (see Methods) and are shown in yellow in C4. Scale bar represents 300 nm. D) The surface-surface contacts between actin and NM2A head group “a” or between actin and NM2A head groups “b” and “c” were measured (“exp”; magenta) and compared to control regions (“ctrl”; grey). Error bars indicate mean +/− SD (n=47 mid-partition events). Statistical significance determined with an unpaired t-test (p=0.004 for “a” and p=<0.0001 for “b&c”). E and F) EGFP-NM2A MEFs untreated (black) or treated with SMIFH2/CK666 (cyan) were imaged with TIRF-SIM (E) or Airyscan (F) and the number of maxima (E) or total filament cluster intensity (F) were measured for 3 minutes following nucleation. Data plotted as mean +/− SEM. n values in parentheses indicate number of filaments. Statistical significance was determined using a Mann-Whitney test. p=0.0385 for (E) and p=<0.0001 for (F). See Fig. S1 for larger fields of view for A and C.

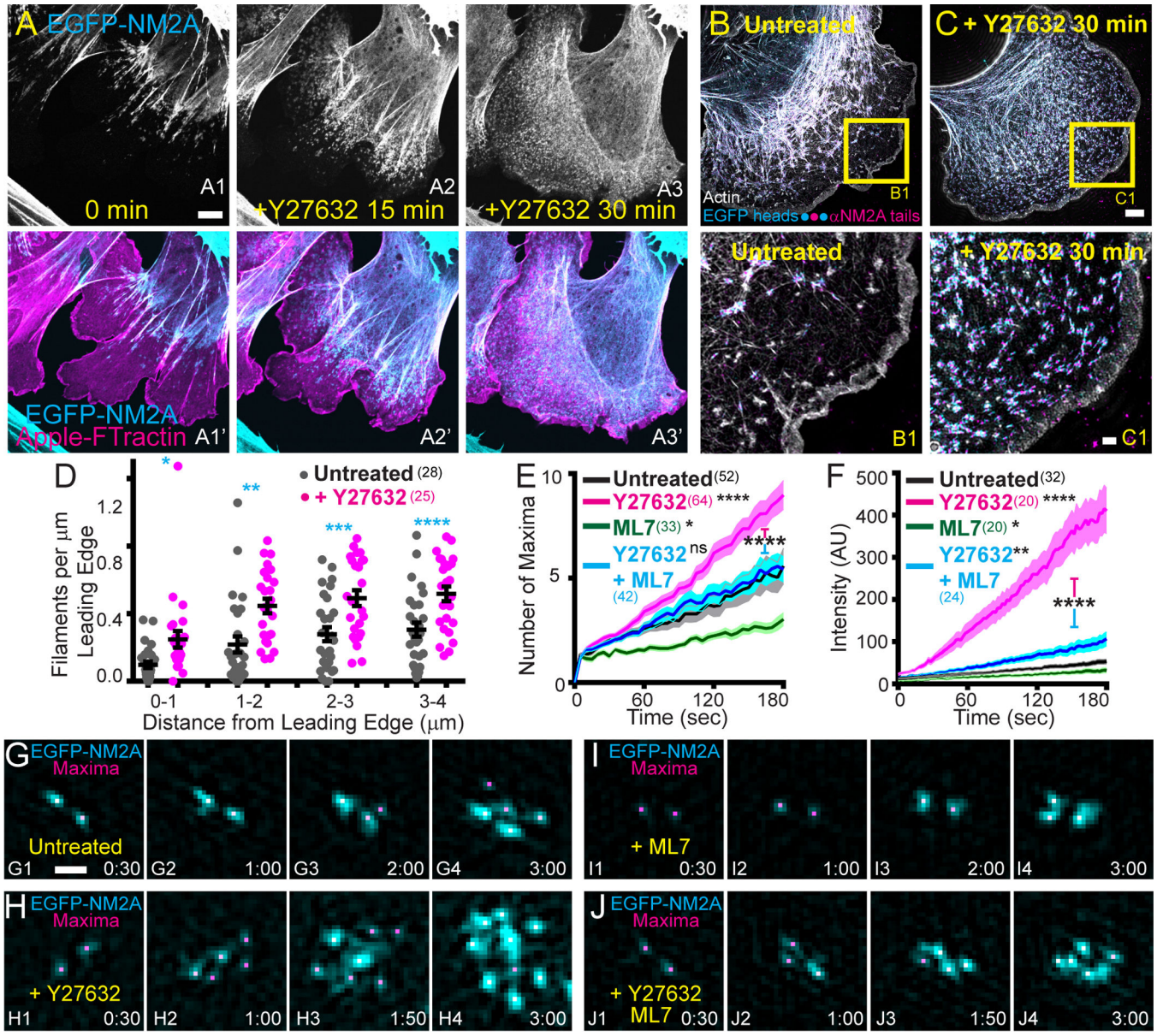

Figure 5. RLC kinase activity regulates NM2A filament partitioning and cluster growth

A) EGFP-NM2A MEF (grey in A1–A3 and cyan in A1'–A3') expressing mApple-F-Tractin (magenta) was imaged with confocal microscopy before (A1 and A1') and during treatment with Y27632 (A2–A3 and A2'–A3'). Time points indicated in minutes. Scale bar in A1 represents 5 µm. See corresponding Video17. This phenomenon was observed in at least 35 cells over 10 experiments with 3 different imaging modalities. B and C) EGFP-NM2A MEFs (cyan) were untreated (B) or treated with Y27632 for 30 minutes (C), fixed, stained with phalloidin (grey), immunostained with αNM2A (magenta), and imaged with 3D-SIM. Z-projections are shown. Yellow boxes in B and C correspond to B1 and C1 insets to the right, respectively. Scale bar represents 5 µm in C and 1 µm in C1. D) NM2A filament coordinates were identified in untreated (grey dots) or Y27632-treated cells (magenta dots), and plotted as a function of distance from leading edge in 1 µm bins. Error bars indicate

mean +/− SEM. Statistical significance determined with an unpaired t-test (p=0.0075 (0—1μm), p=0.0009 (1—2μm), p=0.0014 (2—3μm), p=0.001 (3—4μm)). E and F) EGFP-NM2A MEFs untreated (black), treated with Y27632 (magenta), treated with ML7 (green), or treated with both Y27632 and ML7 (cyan) were imaged with TIRF-SIM (E) or Airyscan (F) and the number of maxima (E) or total filament cluster intensity (F) was tracked for 3 minutes following nucleation. Error bars indicate mean +/− SEM. Statistical significance was determined with a Mann Whitney test, with the p value from comparison to Untreated unless stated otherwise. E) Y27632, p=<0.0001; ML7, p=0.0395; Y27632/ML7, p=0.2133. F) Y27632, p=<0.0001; ML7, p=0.0439; Y27632/ML7, p=0.0064. Asterisks between magenta and cyan bars indicate comparison between Y27632-treated cells and Y27632/ML7-treated cells (p=<0.0001 for (E) and (F)). n values in parentheses indicate number of cells (D) or filaments (E–F). G–J) Representative examples of maxima tracking (magenta) and filament cluster growth rate (cyan) taken from TIRF-SIM images of untreated and drug-treated cells. Treatment indicated in yellow. Time indicated in min:sec. Scale bar in G1 represents 300 nm.

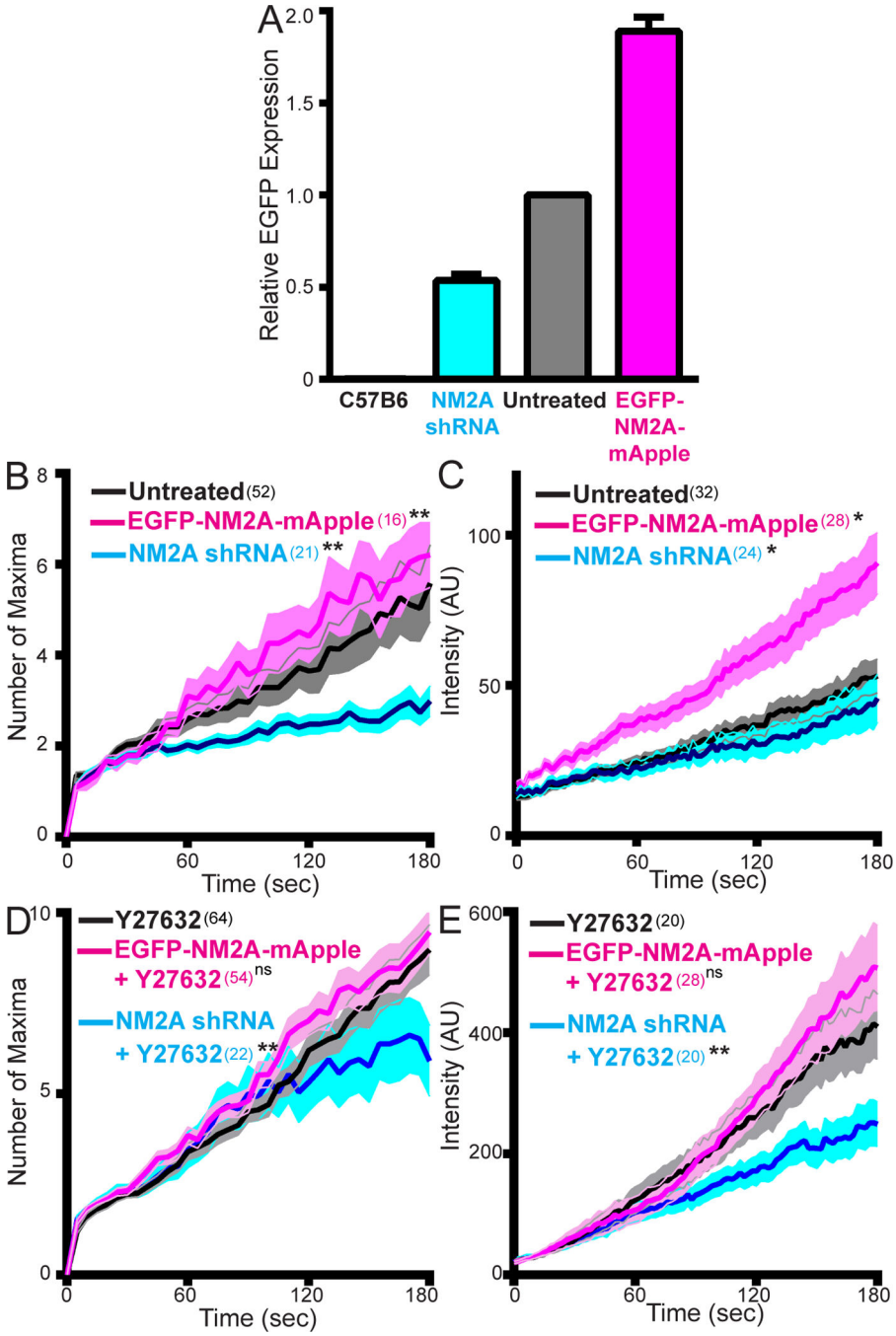

Figure 6. NM2A expression level regulates partitioning and filament growth

A) EGFP-NM2A MEFs untreated (grey) (n=51,950 cells), expressing NM2A shRNA (cyan) (n=29,160 cells), or expressing EGFP-NM2A-mApple (magenta) (n=1,845 cells) were subjected to FACS and relative EGFP expression was analyzed. Control MEFs from C57B6 (n=19,292 cells) mice were used as negative controls. Data plotted as mean +/− SEM. B-E) The three MEF populations shown in (A) were imaged with TIRF-SIM (B and D) or Airyscan (C and E) and the number of maxima (B and D) and total filament cluster intensity (C and E) were tracked for 3 minutes following nucleation. Filament dynamics from NM2A

under-expressing and over-expressing MEFs treated with Y27632 in (D) and (E) were compared to filament dynamics from normal EGFP-NM2A expressing MEFs treated with Y27632. Data plotted as mean +/− SEM. For B–E, n values in parentheses indicate number of filaments. Statistical significance was determined with a Mann Whitney test, with the p value from comparison to Untreated (B and C) or Y27632-treated (D and E). B) EGFP-NM2A-mApple, p=0.0083; NM2A-shRNA, p=0.003. C) EGFP-NM2A-mApple, p=0.0134; NM2A-shRNA, p=0.0433. D) EGFP-NM2A-mApple treated with Y27632, p=0.4341; NM2A-shRNA treated withY27632, p=.0035. E) EGFP-NM2A-mApple treated with Y27632, p=0.36; NM2A-shRNA treated with Y27632, p=0.0262.